Smart Mater. Struct. **20** (2011) 105021 (15pp)

doi:10.1088/0964-1726/20/10/105021

Pneumatic artificial muscles for trailing edge flap actuation: a feasibility study

Benjamin K S Woods¹, Curt S Kothera², Jayant Sirohi³ and Norman M Wereley¹

- ¹ Smart Structures Laboratory, Department of Aerospace Engineering, University of Maryland, College Park, MD 20742, USA
- ² Techno-Sciences, Incorporated, Beltsville, MD 20705, USA
- ³ Department of Aerospace Engineering and Engineering Mechanics, The University of Texas at Austin, Austin, TX 78712, USA

Received 4 March 2011, in final form 13 June 2011 Published 12 September 2011 Online at stacks.iop.org/SMS/20/105021

Abstract

In this study a novel aircraft trailing edge flap actuation system was developed and tested. Pneumatic artificial muscles (PAMs) were used as the driving elements of this system to demonstrate their feasibility and utility as an alternative aerospace actuation technology. A prototype flap/actuator system was integrated into a model wing section and tested on the bench-top under simulated airloads for flight at 100 m s^{-1} (M=0.3) and in an open-jet wind tunnel at free stream velocities ranging up to 45 m s^{-1} (M=0.13). Testing was performed for actuator pressures ranging from 0.069 to 0.62 MPa (10-90 psi) and actuation frequencies from 0.1 to 31 Hz. Results show that the PAM-driven trailing edge flap system can generate substantial and sustainable dynamic deflections, thereby proving the feasibility of using pneumatic artificial muscle actuators in a trailing edge flap system. Key issues limiting system performance are identified, that should be resolved in future research.

S Online supplementary data available from stacks.iop.org/SMS/20/105021/mmedia

(Some figures in this article are in colour only in the electronic version)

Nomenclature

OD outer diameter

k linear spring constant

L uninflated actuator length

M Mach number

p actuator internal air pressure

R actuator radius

 $S_{\rm f}$ planform area of flap

v free stream velocity

 α angle of attack

 δ flap deflection angle, positive downwards

 ΔL change in actuator length

 ΔR change in actuator radius

 θ deflection angle of moment arm for

spring loading setup

 λ contraction ratio

 ρ density of air

 $c_{\rm f}$ flap chord

 $c_{\rm h}$ total hinge moment coefficient

 $c_{h_{\alpha}}$ hinge moment coefficient due to angle of attack

 $c_{\mathrm{h}_{\delta}}$ hinge moment coefficient due to flap deflection

 λ_0 actuator free contraction ratio

 $F_{\rm bl}$ actuator blocked force

1. Introduction

1

The design and optimization of aircraft control surfaces has long been an important area of research in the aerospace community. Obtaining effective aircraft control authority has required the development of powerful actuator technologies. However the need for powerful actuators must be balanced by stringent weight and reliability requirements. These design constraints have led to the widespread adoption of two primary technologies, hydraulic actuation systems and electric motors. Operating under high pressure, hydraulic actuators are capable of producing large, sustainable control forces, but their disadvantages include the weight penalty associated with bulky actuator components, dense operating fluid, and extensive high pressure plumbing and fittings that are prone to leakage. Electric motors are also capable of generating large control forces at high actuation rates, but

often their size, power requirements, and weight limit their utility. The drawbacks of these existing actuation schemes has in recent years led to consideration of alternative actuators with potentially improved performance characteristics. This technology push was largely due to the development of active (smart) materials, such as piezoelectric ceramics [1–5], shape memory alloys [6–9] and magnetostrictives [10, 11]. Accordingly, significant effort has been put into actuation schemes that employ active materials, but these have so far proven to be limited in output performance for full-scale vehicles. For instance, piezoelectric materials have high force, but low stroke, and shape memory alloys have a dynamic barrier in actuation bandwidth. These limitations are also present even when mechanisms designed for mechanical advantage [12], and for frequency rectification, are employed.

Thus, new types of actuators should be developed to overcome the issues outlined above. Pneumatics represent an actuation technology that may be able to overcome the noted limitations of other actuation devices. Specifically for unmanned aerial vehicles (UAVs), conventional pneumatic piston actuators can successfully actuate a variety of control surfaces [13], including camber augmentation [14], changes in sweep [15], and telescopic changes to span [16, 17]. A second class of pneumatic actuators referred to as pneumatic artificial muscles (PAMs) [18] has also shown great promise. Most notable in this category is the McKibben actuator, which has been well studied for low bandwidth (<1 Hz) robotics applications, but has not been considered for aerospace applications requiring higher bandwidth. McKibben actuators consist of an elastomeric bladder (most commonly silicone or latex rubber) encased in a helically braided sleeve and sealed at both ends. One end has an air fitting attached to allow for pressurization (inflation) and exhaustion (deflation) of the actuator. As such, they are relatively simple light weight devices. Furthermore, they can generate significant levels of force (6000 N) [19] and contraction (30% or more of original length) at modest actuation pressures (0.69 MPa) [20]. High force and low weight also result in impressive energy densities [19, 21]. For example, actuator specific energy ratios of nominally 300 J kg⁻¹ can be achieved with commercially available PAM actuators [19], which is significantly better than energy densities of 1-10 J kg⁻¹ typical of piezoelectrics and 3 J kg⁻¹ typical of magnetostrictive actuators [22]. Although PAMs do not have an energy density as high as the 800 J kg⁻¹ energy density typical of shape memory alloys (SMA), PAMs have much faster response times and so are better suited to dynamically driving control surfaces [22]. PAMs also have excellent specific power, on the order of 0.5–2 kW kg⁻¹ [23].

The operating principle of McKibben type pneumatic artificial muscles, hereafter referred to simply as PAMs, is as follows. When the bladder is pressurized with air, it expands in the radial direction, pressing outward on the braided sleeve. This forces the braided sleeve to also increase in diameter through reorientation of the helical braid. However, the fixed length of the braided sleeve fibers generates a contractile force and causes a reduction in the overall length of the muscle. Figure 1(a) shows a diagram of this process. The maximum operating pressure, hence, the maximum actuation force, is

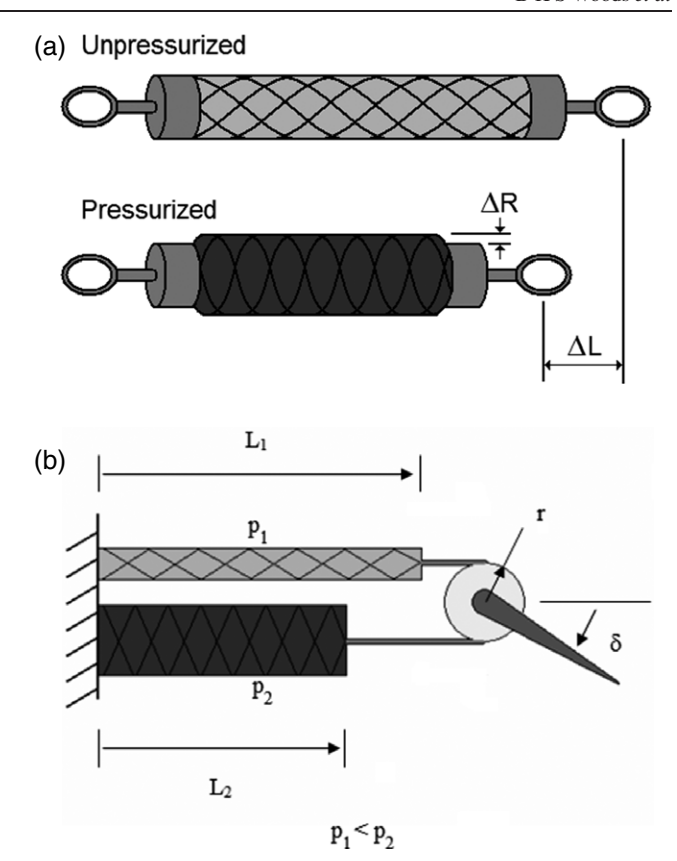


Figure 1. PAM actuation overview. (a) Operating principle. (b) Antagonistic PAM pair driving flap.

often pressure limited: (1) high performance pneumatic control valves are often limited to handling nominal pressures as high as 1–1.4 MPa (150–200 psi), and (2) the risk of the bladder squeezing through the braided sleeve and rupturing, although at much higher nominal pressures of 7 MPa (1000 psi), in our own tests not reported here. PAMs are intrinsically a unidirectional actuator capable of producing significant force levels only in contraction, so that PAMs are similar to natural muscles [24]. If bi-directional motion is desired, two pneumatic muscles can be configured as an antagonistic pair and operated alternately to produce bi-directional rotational motion about a hinge as in figure 1(b). Such a biomimetic arrangement is capable of actuating aircraft control surfaces.

The objective of this study is to design and build a prototype PAM-driven aerodynamic control surface, that is, a trailing edge flap, and to evaluate its performance in terms of the achievable flap deflection range and frequency response. A 0.61 m (24 in) span of a 0.53 m (21 in) chord NACA-0012 airfoil was chosen as a representative wing section. A 15% chord flap with a span of 25.4 cm (10 in) was installed at the center of the trailing edge of the wing section. An antagonistically arranged pair of PAMs, having an outer diameter of 1.27 cm (0.5 in) and an active length of 8 cm, drove the flap. The active length here is defined as the length of the PAM between its two end fittings. The system was tested on the bench-top for aerodynamic loading, simulated by a spring, associated with 100 m s⁻¹ (M = 0.3) flight at 6° angle of attack. Additional testing was performed in a free-jet

wind tunnel at wind speeds up to 45 m s^{-1} (M=0.13). In both cases the system was tested at actuator pressures ranging from 0.069 to 0.62 MPa (10–90 psi) and flapping frequencies ranging from 0.1 to 31 Hz. These test conditions were chosen to be relevant to a range of potential applications, including subsonic UAVs, helicopter rotor blades, and wind turbine blades.

2. System design

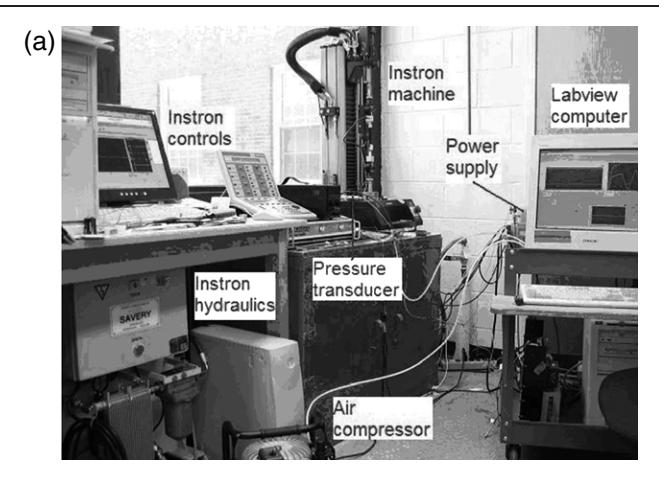
2.1. Actuator development

2.1.1. PAM construction. To realize a trailing edge flap actuation system, an appropriately sized PAM actuator was developed and characterized. Actuator sizing was driven primarily by geometric constraints. The system was designed such that an antagonistic pair of PAMs was stacked vertically (in the thickness direction of the airfoil), and enclosed within the rear 65% of the airfoil section. This imposed several design constraints on PAM diameter and length. The diameter was limited by requirement that the inflated diameter of the two PAMs fit within the airfoil thickness. The length was constrained to be less than 65% of the airfoil section, however, other constraints further reduced allowable PAM length: the rear 15% of the airfoil was taken up by the flap itself and allowances were made for PAM mounting hardware including end fittings, turnbuckles, and a moment transfer mechanism. To fulfil all of these constraints for the chosen 0.53 m (21 in) chord NACA-0012 airfoil, the outer diameter was limited to 1.27 cm (0.5 in), and the maximum active length to 8 cm. In order to maximize performance, both the diameter and length of the actuator were selected to be these maximum values.

The PAMs built to fit within this envelope were made from latex tubing having an outer diameter (OD) of 1.27 cm (0.5 in) with a 0.16 cm (1/16 in) wall thickness surrounded by a braided sleeve made from 0.25 mm filaments of PET plastic. When pulled taught around the latex tubing, the filaments of this sleeve form an angle of $\pm 43^{\circ}$ relative to the long axis of the PAM. The open ends of the bladder/braided sleeve were sealed around end fittings using a wire wrapping method adopted from Images SI Inc. (www.imagesco.com). The PAMs were attached to test equipment and the experimental model using threads machined into the end fittings. Furthermore, one end fitting on each PAM was hollow to enable pressurization of the actuator.

2.1.2. Experimental characterization. To characterize the performance of the PAMs, the specimens were tested on an Instron 8841 servohydraulic table-top material testing machine. This machine applied load to the PAM specimen while recording force and displacement with a load cell and LVDT, respectively. A load ramp profile was performed to allow collection of force versus displacement data over the full working range of the actuator. This test setup can be seen in figure 2.

Using this setup, we generated quasi-static actuator load lines for both PAMs. The force versus time and displacement versus time data that was collected from the Instron was



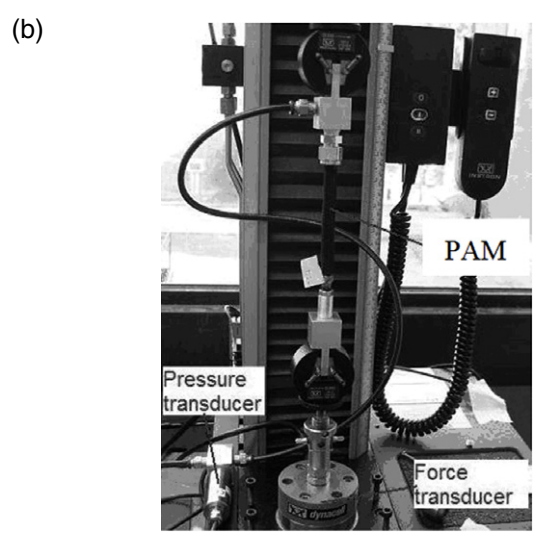


Figure 2. PAM characterization setup. (a) Test area overview. (b) PAM mounted on Instron testing machine.

combined to show force versus displacement in quasi-static actuator load lines. PAM displacement data was non-dimensionalized by defining a contraction ratio, λ , as below:

$$\lambda = (L - \Delta L)/L. \tag{1}$$

Quasi-static actuator load lines were measured for each actuator at pressures ranging from 0.069 MPa (10 psi) to 0.62 MPa (90 psi) in 0.14 MPa (20 psi) increments. A typical characterization of actuator force versus contraction ratio is shown in figure 3 for the set of discrete values of pressure. Note that for a given pressure, the maximum force occurs while the PAM is constrained to not contract; hence, this force is known as the blocked force, F_{bl} . Force decreases with increasing contraction (decreasing λ). Force eventually reduces to a value of zero, which is where the contraction reaches its maximum value known as the free contraction, λ_0 . Also note that increasing actuator pressure causes an increase in both blocked force and free contraction. These performance traits are similar to those reported elsewhere [20, 24–26]. Operational pressures in this study were limited to 0.62 MPa (90 psi) in order to increase fatigue life [27].

Another characteristic of PAMs is that the blocked force generated at a given pressure can be increased by inducing a

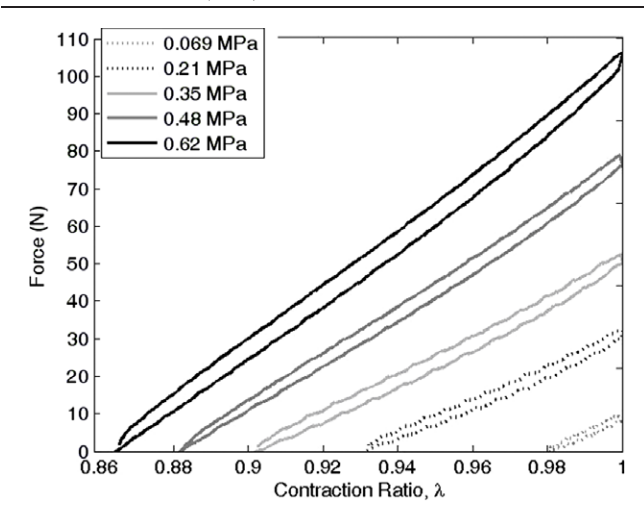


Figure 3. Typical PAM force–contraction characteristics (1.27 cm OD, 10.2 cm length).

tensile pre-strain on the actuator. For instance, a 150% increase in the force available was observed for the PAM having an outer diameter (OD) of 1.27 cm (0.5 in) and length of 10.2 cm (4 in). Figure 3 shows that the blocked force generated at 0.62 MPa (90 psi) by this actuator was approximately 107 N, while adding a 12% pre-strain increased the blocked force to almost 267 N. Adding pre-strain increases the force because of the intrinsic stiffness of the actuator. Because both PAMs are initially pre-strained the same amount in the antagonistic actuator configuration, these force augmentations balance, retaining the desirable zero degree flap deflection neutral point.

2.2. Flap sizing and design

The 15% chord flap size was chosen as representative of a trailing edge flap that might be employed as an aileron, elevator, elevon, rudder, rotor blade trailing edge flap, or wind turbine trailing edge flap. The flap span of 25.4 cm (10 in) was chosen to scale aerodynamic loads so that a single antagonistic PAM pair could be used. Additionally, the width of the air flow from the free-jet wind tunnel in which our experiments were conducted was approximately 50.8 cm (20 in) wide, so limiting the flap span to 25.4 cm (10 in) helped ensure a uniform flow in the region of interest.

Predictions of the quasi-static hinge moments were made for a design condition of M=0.3, $\alpha=6^\circ$, and $\delta=\pm 10^\circ$. This design condition was chosen as being representative of a mid-span active flap on a helicopter rotor blade, a UAV control surface, or a trailing edge flap at the tip of a large horizontal axis wind turbine. The required hinge moment under these flow conditions was desired to allow for estimates of system performance. A quasi-static, incompressible analysis was used. The total aerodynamic hinge moment can be determined as a combination of hinge moment due to angle of attack and hinge moment due to flap deflection as below:

$$c_{\rm h} = c_{\rm h\alpha}\alpha + c_{\rm h\delta}\delta. \tag{2}$$

Values for these coefficients were determined from tabulated experimental data [28, 29]. The hinge moment was determined



Figure 4. PAMs fabricated for the wind tunnel test article.

as below:

$$H = \frac{1}{2}\rho v^2 S_{\rm f} c_{\rm f} c_{\rm h}. \tag{3}$$

Using this method, it was predicted that a hinge moment of 1.9 N m would be required to sustain a positive 10° deflection at the design condition. To deduce the required actuator force, the moment arm between the actuator and flap hinge was needed. The moment arm is dependent on the actual design of the force transfer mechanism. Due to the thinness of the airfoil at the 85% chord location (22 mm) and the desire to incorporate ball bearings into the rotating components of this mechanism, the moment arm was limited to a maximum of 6.9 mm. With this moment arm, an actuator force of approximately 276 N is required to generate a 1.9 N m hinge moment. It was expected that this actuator force level could be achieved by incorporating a 12% pre-strain in the PAMs having an OD of 1.27 cm (0.5 in). One advantage of the small moment arm used was that the PAM contraction required to deflect the flap 10° was very small. Using the arc length equation with the small angle assumption ($\Delta L = r\theta$), the required contraction was only 2.1 mm, or 2.6% of the PAM active length. Although actuator force decreases with contraction, the small required deflection implied that a large majority of the force would still be available at 10° deflection (90% for a PAM with an active length of 8 cm and 12% pre-strain). The PAMs used in this experiment have an overall length of 10.2 cm, but have an active length of only 8 cm. Recall that the actuation force of the PAM is determined by its active length, not overall length. The active length is defined as the distance between the inner faces of the end fittings of the PAM. This is the only portion of the actuator that inflates and contributes to the generation of force. These PAMs, shown in figure 4, each having a mass of 37 g with air fittings and mounting brackets installed.

Once the actuator size was chosen, then the flap mechanism was designed. The two PAMs were mounted one above the other on the inside face of the wing spar. This arrangement, seen in figure 5, ensures that the actuation forces cause a pure rotational moment about the flap spar. A moment block was mounted directly to the flap spar. The actuator forces were transferred to this moment block via pivot bars connected

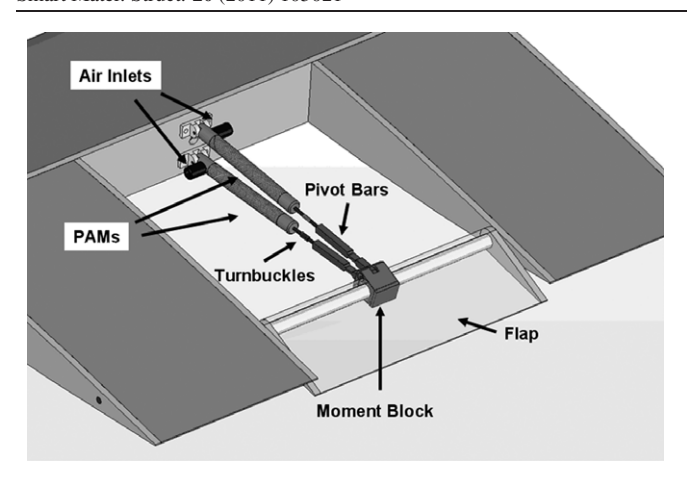


Figure 5. Flap/actuator system design.

to the contracting ends of the PAMs. Force transfer occurs via a 3.2 mm steel shaft embedded in the pivot bars that rotates in stainless steel ball bearings embedded in the moment block. This provided a rotating interface capable of handling the static and dynamic forces of the system.

From the results of our actuator characterization it was determined that the ability to pre-strain the actuators in tension was needed. To allow this, a turnbuckle was placed between the pivot bars and the actuator end fittings. These turnbuckles are right hand threaded on one end and left hand threaded on the other. This allows for the nominal distance between the pivot bars and actuators to be changed. This is useful both for adding tensile pre-strain to the system and for compensating for slight differences in the length of the two PAMs.

The flap itself consisted of two plies of 0.38 mm preimpregnated fiberglass/epoxy around an extruded polystyrene foam core. A 1.27 cm outer diameter aluminum tube formed the flap spar. A flanged ball bearing at either end of this tube allowed the flap to rotate freely around a 6.4 mm steel rod that runs through the entire test section. The flap was reinforced with two 6.4 mm thick aluminum end plates mounted onto the flap.

2.3. Test article development

A wing model was designed around the actuator/flap assembly to show how such a system could be integrated into an aircraft. The wing model was designed so that it could be tested in the free-jet wind tunnel. Sensors were incorporated into this test article to measure pressure inputs, PAM actuation forces, and flap angle.

2.3.1. Wing model construction. The wing structure was composed of six primary components: two end plates, one mounting spar, two flap support ribs, and one flap pivot rod. These components, with the exception of the flap pivot rod, were 6061-T6 aluminum and were CNC machined from 6.4 mm plate. The flap pivot rod was a length of precision ground 6.4 mm steel rod. A fiberglass/epoxy skin was built around this frame to create a smooth outer surface for aerodynamic testing. Figure 6(a) shows the basic frame with

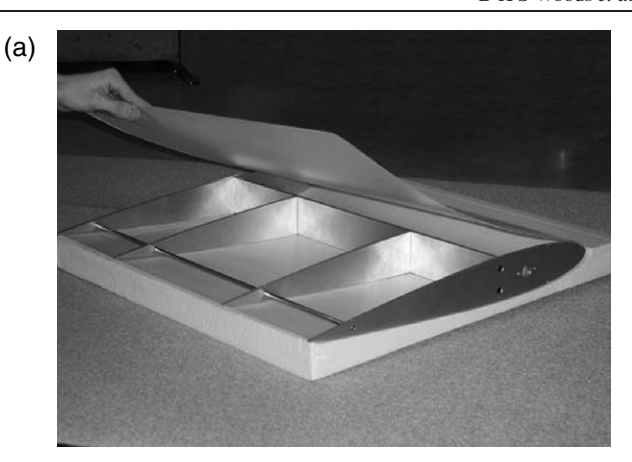




Figure 6. Wind tunnel test section construction. (a) Internal view of aluminum frame. (b) Frame with skin in place.

the skin lifted up to expose the individual components and figure 6(b) shows the skin encasing the frame.

As on the flap, the wing section skin consisted of two plies of 0.38 mm pre-impregnated fiberglass/epoxy. The skin in front of the mounting spar was reinforced with a sandwich structure consisting of two 0.76 mm fiberglass layers separated by 3.2 mm of foam. This greatly increased the stiffness of the leading edge to allow it to withstand pressures generated during aerodynamic testing. Foam inserts were placed between the upper and lower skin surfaces at the rear of the wing, excluding the central 25.4 cm (10 in) section that was occupied by the flap/actuator assembly. These inserts were attached to the skin to reduce panel vibration during testing. To allow easy access to the PAM system, a hatch was cut into the upper surface of the skin directly above the PAMs. The seams of the hatch were taped down during the wind tunnel test.

2.3.2. Sensor integration. Several sensors were used to monitor the performance and to track the response of the trailing edge flap system. First, a non-contact rotary position sensor (Midori Precisions Co. Model QP-2HC) was installed to measure the flap deflection angle δ . Secondly, 0°/90° tee-rosette strain gauges from Vishay Micro-Measurements were incorporated into the pivot bars to provide a means of measuring the forces generated by the PAMs. These were mounted to the top and bottom of a necked down length of each



Figure 7. The $80/20^{\$}$ test stand with assembled wing section.

pivot bar to create a complete full-bridge strain gauge circuit to cancel out any bending moments. Necking down the pivot bar increased local strains; thereby increasing measurement sensitivity. Strain gauge output voltage was directly calibrated to force in the pivot bars by mounting each bar in the Instron material test machine and performing load ramps while measuring gauge voltage. Finally, two pressure transducers (Omegadyne Model PX209-200G5V) were integrated into the pneumatic supply circuit. The internal pressure of each PAM was the desired measurement for this testing, but it was not possible to install transducers inside of the actuator body due to the small size and design of the actuators. Therefore, the transducers were installed just upstream of the PAMs, as close as possible to the end fittings. Pressure measurement at this location is a fairly accurate approximation of the actual internal PAM pressure.

3. Test section development

3.1. Bench-top test setup

A test stand was developed for bench-top and free-jet wind tunnel testing (figure 7). The frame of the test stand was built from 80/20[®] aluminum extrusions that were bolted together. The wing is mounted, and pivots, about its quarter chord point via cylindrical extensions of the end plates supported by needle bearings. These extensions are hollow to allow the instrumentation wires and air tubes to be fed out of the test section, while the bearings permitted the angle of attack of the wing to be changed. A clamping mechanism was employed to fix the airfoil section at each chosen angle of attack. Not shown in the figure are the acrylic side walls used during wind tunnel testing to produce as close to a 2D flow as was possible in this situation.

For simulating aerodynamic loads during bench-top testing, a suitable loading mechanism had to be implemented. As mentioned above, the flap hinge moment was estimated to be approximately 1.9 N m at 10° of flap deflection. To create the desired torsional stiffness, linear tension springs

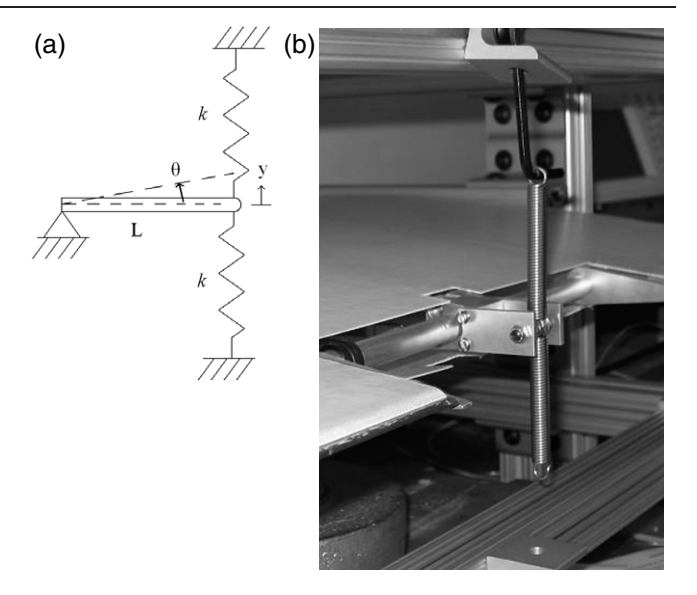


Figure 8. Spring loading mechanism. (a) Schematic diagram. (b) Partially assembled.

were mounted at a known moment arm from the center of flap rotation.

The spring design is based on the diagram shown in figure 8(a). For the design condition, the required torsional spring constant is 0.19 N m/deg. The length of the moment arm was fixed at 3.81 cm to limit the required spring deflections. For 10° of rotation, it can be assumed that $\sin(\theta) = \theta$, and thus spring deflection $y \approx \theta L$.

Each degree of rotation then corresponds to 0.67 mm of motion. The total required linear spring stiffness can then be calculated according to:

$$0.19 \frac{\text{N m}}{\text{deg}} \frac{1}{38.1 \text{ mm}} \frac{1 \text{ deg}}{0.67 \text{ mm}} = 7443 \frac{\text{N}}{\text{m}}.$$
 (4)

As shown in figure 8(a), the stiffness of the system is 2k because the spring stiffnesses are additive in parallel. This yielded a design spring constant of $k=3722 \text{ N m}^{-1}$ for each spring. Commercially available tension springs were found that came within 3% of this stiffness. These can be seen in figure 8(b), partially assembled with the mechanism. Note that the spring tensioning screws were not yet incorporated into the system shown in the figure, but when installed they rigidly fixed the shown free ends of the springs to the frame of the test stand.

The laboratory equipment used during both bench-top and wind tunnel testing is shown in figure 9. In this arrangement, a Jun-Air/Newport compressor supplied pressurized air to the accumulator, whose built-in regulator could be adjusted to the desired pressure setting prior to each experiment. Pressurization of the actuators was regulated by the shown control circuit that controlled the operation of two solenoids linked to the PAMs. This circuit simultaneously pressurized the active PAM while venting the passive PAM. This was accomplished with two 50% duty cycle square waves 180° out of phase. The frequency of these square waves was controllable via user input to a LabVIEW Data Acquisition

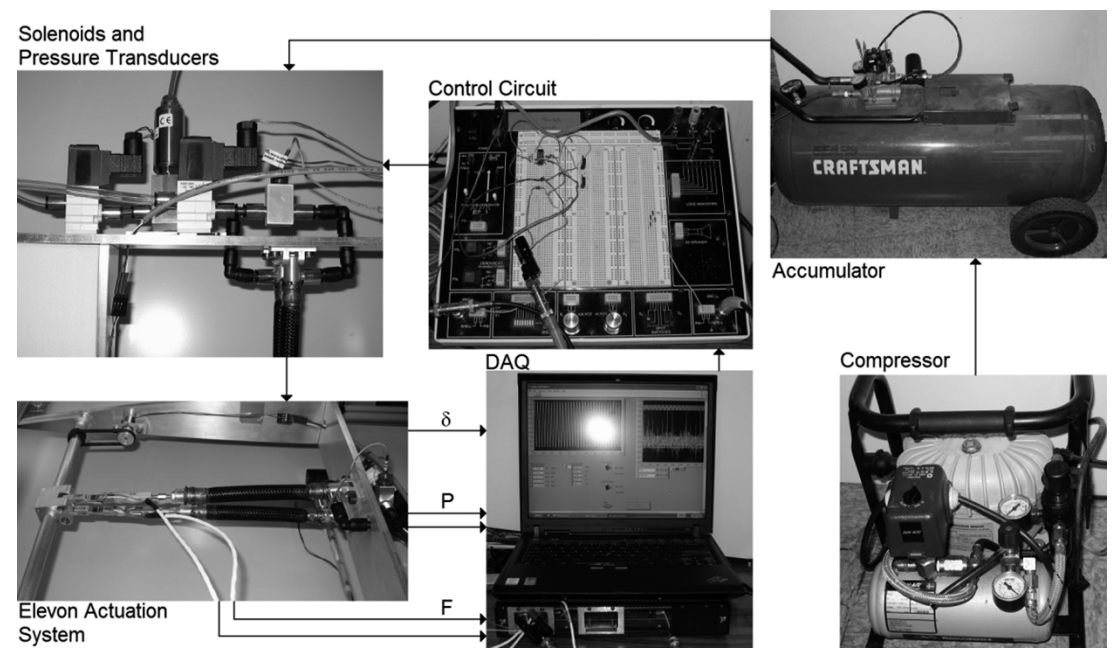


Figure 9. Laboratory setup for system evaluations.

System. With input pressure and operating frequency set, the flap system was actuated and data from all five sensors was collected, with sampling performed at 1.0 kHz.

3.2. Wind tunnel test setup

The primary instruments and components of the free-jet wind tunnel experiment were the same as those detailed for the bench-top experiments. However, the loading springs used in the bench-top experiments were eliminated. Figure 10 shows the prototype system oriented in the test stand and bolted in place in front of the free-jet. The angle of attack was set at 6° by bolts placed in holes drilled through the acrylic side walls. The air line enters the left side of the prototype system through a hole at the 1/4-chord position and the instrumentation wiring enters through the right side.

4. Results and analysis

4.1. Performance measurements for the unloaded system

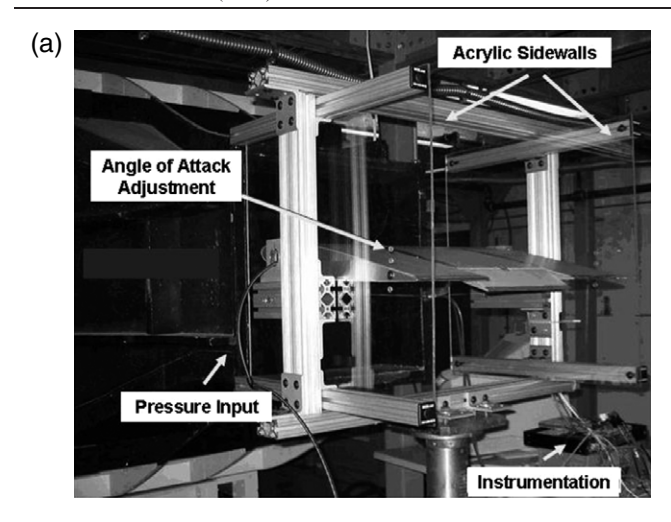
Using the above-mentioned testing equipment, the unloaded (no springs or aerodynamic loading) system response was experimentally characterized from 0.069 MPa (10 psi) to 0.62 MPa (90 psi) in 0.069 MPa (10 psi) increments (nine total pressures) and over the frequency range of 0.1–31 Hz with square wave inputs. Two frequencies below 1.0 Hz (0.1, 0.5 Hz) were tested first and then data was captured at all the odd frequencies between, and including, 1.0–31 Hz (18 total frequencies).

The effects of pre-straining the actuators were also investigated. Due to our choice of sensors we could only monitor the force in the actuators, but not their displacement. This allowed application of a known pre-tension, but not a

known pre-strain. The force level required to cause a 12% prestrain in the PAMs was measured to be 100 N on the Instron, which was used to calibrate the pre-tension in the wing model. Two other values of pre-tension were tested to examine the effect of pre-tension on flap/actuator system performance. The three levels tested were 10, 60, and 100 N.

Figure 11 shows sample time responses for downward and upward flap deflections at 10 N of pre-tension. The angle sensor data is shown in the upper two plots, followed by the pressure and force measured for the top actuator, and then the pressure and force for the bottom actuator. Here $F_{\rm B}$ is the force in the bottom actuator, $F_{\rm T}$ the force in the top. Similarly, $P_{\rm B}$ is the bottom PAM pressure and $P_{\rm T}$ the pressure in the top. This 0.1 Hz case effectively gives the system response to step inputs, and is useful because it best corresponds to the quasistatic deflection condition used in performance predictions and system design.

The two different response characteristics for the system as shown in figure 11, flap down and flap up, are essentially mirror images of one another. The one exception to this is the response for the bottom load cell, $F_{\rm B}$, which shows significantly more noise than $F_{\rm T}$, in addition to an added non-decaying frequency content. Both of these attributes are believed to be a result of damage to the load cell and/or some undiagnosed interference. The top and bottom actuators trade antagonistic roles, yet comparison of either the active or passive actuator data between cases shows a nearly identical response. For instance, in the flap down case, the bottom actuator is active, with actuator pressure shown as $P_{\rm B}$ in the left column. This shape is identical to the active actuator pressure for the flap up case, given by $P_{\rm T}$ on the right. Thus the data for a single actuator can be used as a representative case. For brevity and to remove the effect of the noise in the bottom load cell, only the data for the upper PAM actuator will be discussed for the remainder of this paper.



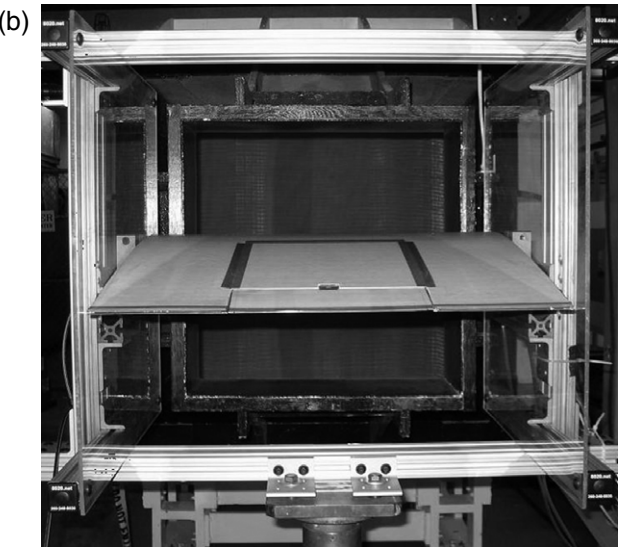


Figure 10. Model wing section in free-jet wind tunnel. (a) Overview of installed system. (b) Rear view. A video of the trailing edge flap in operation during a free-jet wind tunnel test at the University of Maryland, which was performed at a wind speed of 30 m s⁻¹ is provided in the supplementary data (available at stacks.iop.org/SMS/20/105021/mmedia).

While the representative 0.1 Hz case in figure 11 illustrates a step response, figure 12 has been included to show how the wave shape changes with frequency. Appearing in this figure are two periods of time data for the flap deflection angle (figure 12(a)) and the corresponding actuation force (figure 12(b)) at frequencies that span the range tested for this system. It can be seen that the square wave input is still closely followed at 1.0 Hz, but as the frequency increases, the wave shape becomes distorted. The deflection angle progresses from a square wave to nearly a sinusoidal wave, while the force measurement changes to a nearly triangular waveform. Also seen is that the amplitude of the waves tends to decrease with increasing frequency.

We will now investigate the effects of loading, pre-tension, frequency and pressure on system performance. Figure 13 shows flap deflection angle versus solenoid driving frequency. This set of results, along with the similar pressure and force

results to come, shows the maximum downward (positive) deflections averaged over each period of collected data. The system performance was symmetric about $\delta = 0^{\circ}$ for nearly all tested cases, so that only the positive deflections are shown here for clarity. As actuation pressure increases, the actuator force increases, and overall system stiffness also increases. This causes a noticeable shift in resonance to higher frequencies with increasing pressure in figure 13(a), eventually peaking beyond the range of tested frequencies for pressures above 0.35 MPa and 10 N pre-tension. PAM stiffness is pressure dependent, so it stands to reason that the natural frequency of the system would also increase with pressure. Apparent around the 10–15 Hz range in all three pre-tension cases is a reduction in achievable flap deflection angle. In the 10 N case, there is a slight reduction for all pressures that is subsequently masked above 20 Hz by resonance. At 60 N and 0.62 MPa, the flap angle ranges $\pm 15^{\circ}$ (0.1 Hz) to $\pm 10^{\circ}$ (31 Hz) and at 100 N, the angle ranges from $\pm 10^{\circ}$ (0.1 Hz) down to $\pm 5^{\circ}$ (31 Hz) in a similar manner. Comparing figures 13(a)– (c), the most obvious difference is a substantial reduction in overall deflection achieved with increasing pre-tension. This investigation shows that, while applying pre-tension to the PAMs does increase their active force, unfortunately, applying pre-tension fails to increase flap deflection.

To further illustrate the effect of pre-tension on achievable flap angle deflection, the measured actuation forces are displayed in figure 14. The upper set of curves in each plot represent the actuator force while active (pressurized), and the lower curves represent the actuator force while passive (exhausted). The higher pre-tension cases do generate higher active PAM forces (the maximum force produced at 0.62 MPa (90 psi) for each of the three increasing pre-tensions is respectively 93.4, 156, and 218 N), but the passive force also increased, as seen in the upward shift, which limits flap deflections. Essentially, the active (pressurized) PAM must overcome the force exerted by the passive (deflated) PAM. Therefore, increasing the pre-tension on both PAMs does not benefit the flap deflection.

Another noticeable trend at all pre-tension levels in figure 14 is a decrease in active actuator force and a slight increase in passive actuator force with increasing frequency. Following the same pattern as was seen in the deflection angle of figure 13, the trend begins at approximately 10–15 Hz for each pre-tension case and pressure. Examining the actuator pressures shown in figure 15, a parallel trend can be seen.

In figure 15, the upper curve for each pressure setting is the maximum (pressurized) and the lower curve is the minimum (exhausted). The pre-tension appears to have no effect on the measured pressure. Internal PAM pressure is dependent on the source of compressed air, properties and geometry of the supply lines, and solenoid operating frequency. These results not only show that the desired pressure level cannot be attained as frequency increases (the lines would be horizontal at each respective actuation pressure in that case), but also that complete exhaustion of the passive PAM does not occur at higher frequencies. For instance at 31 Hz, the supposed 0.62 MPa pressure peaks only at 0.35 MPa and exhausts to between 0.069 and 0.10 MPa. This reduced

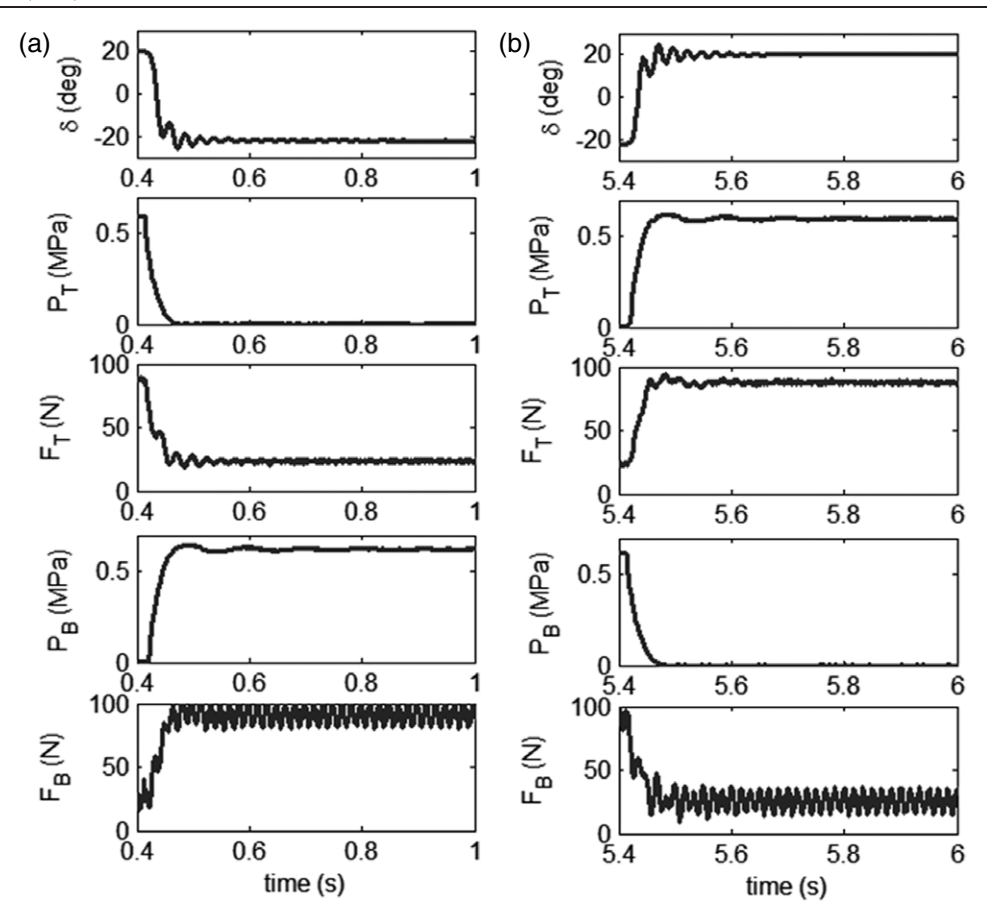


Figure 11. Sample time responses of system measurements—(0.62 MPa, 0.1 Hz, 10 N). (a) Flap up. (b) Flap down.

pressure range is likely the main cause of drop off in the system performance with increasing frequency shown in figures 13(a)–(c); note that the frequencies of the declining pressure and performance coincide (\sim 10 Hz). The decreased pressure range also accounts for the decline in active actuator force and increase in passive actuator force seen in figures 14(a)–(c).

As mentioned above, the pressure response in the PAM actuators is dependent on the flow characteristics of all the upstream hardware. The roll-off in pressure seen here at high frequency identifies a performance limit of the pneumatic system as configured, where flow rate has reached a maximum and continuing to increase the operational frequency causes the noticed decrease in flap deflection. Hence, if the same large deflections at low frequency were desired at higher frequency, one method to improve system response would be to install higher flow rate pneumatic components.

4.2. Performance measurements under simulated aerodynamic loading

For the loaded bench-top experiments, the same laboratory setup was used as in the unloaded tests (figure 7), except for the addition of the loading springs emulating aerodynamic loads at M=0.3 and the associated attachment hardware. Testing was performed at the same 18 frequencies, 9 pressures, and 3 pretensions as the unloaded testing case.

While the loaded frequency response for force and pressure are very similar to those for unloaded operation, as

shown in figures 14 and 15, the response for flap deflection versus frequency exhibits quite different characteristics. Figure 16 shows the dependence of flap deflection on pressure and frequency for increasing levels of pre-tension while operating at the simulated design load. It is interesting to note the pre-tension seems to have little influence on the achievable flap deflection for the loaded case, while it was shown to decrease with increasing pre-tension in the unloaded condition. At the maximum pressure of 0.62 MPa and the lowest frequency of 0.1 Hz, an approximation of the static condition, about $\pm 4.5^{\circ}$ deflection is achieved for all three pre-tension settings. Then there is a gradual drop off up to 20 Hz, where a more noticeable reduction occurs, after which the flap is able to operate between approximately $\pm 2^{\circ}$.

The data of figure 16 is shown in a different form in figure 17, where results at 0.62 MPa are compared for all three pre-tensions. These results highlight the trends discussed previously. That is, for the full load case, the level of pre-tension has little effect on the attainable flap deflections since measurements from all three test cases are shown to overlay each other. Also as discussed previously, the decreased performance with increasing frequency is attributable to flow rate limitations in the pneumatic components. These bench-top results establish the relative independence of actuator force and pressure responses from the loading condition. This is expected since actuator force is driven primarily by internal pressure; and pressure is determined by the pneumatic supply system.

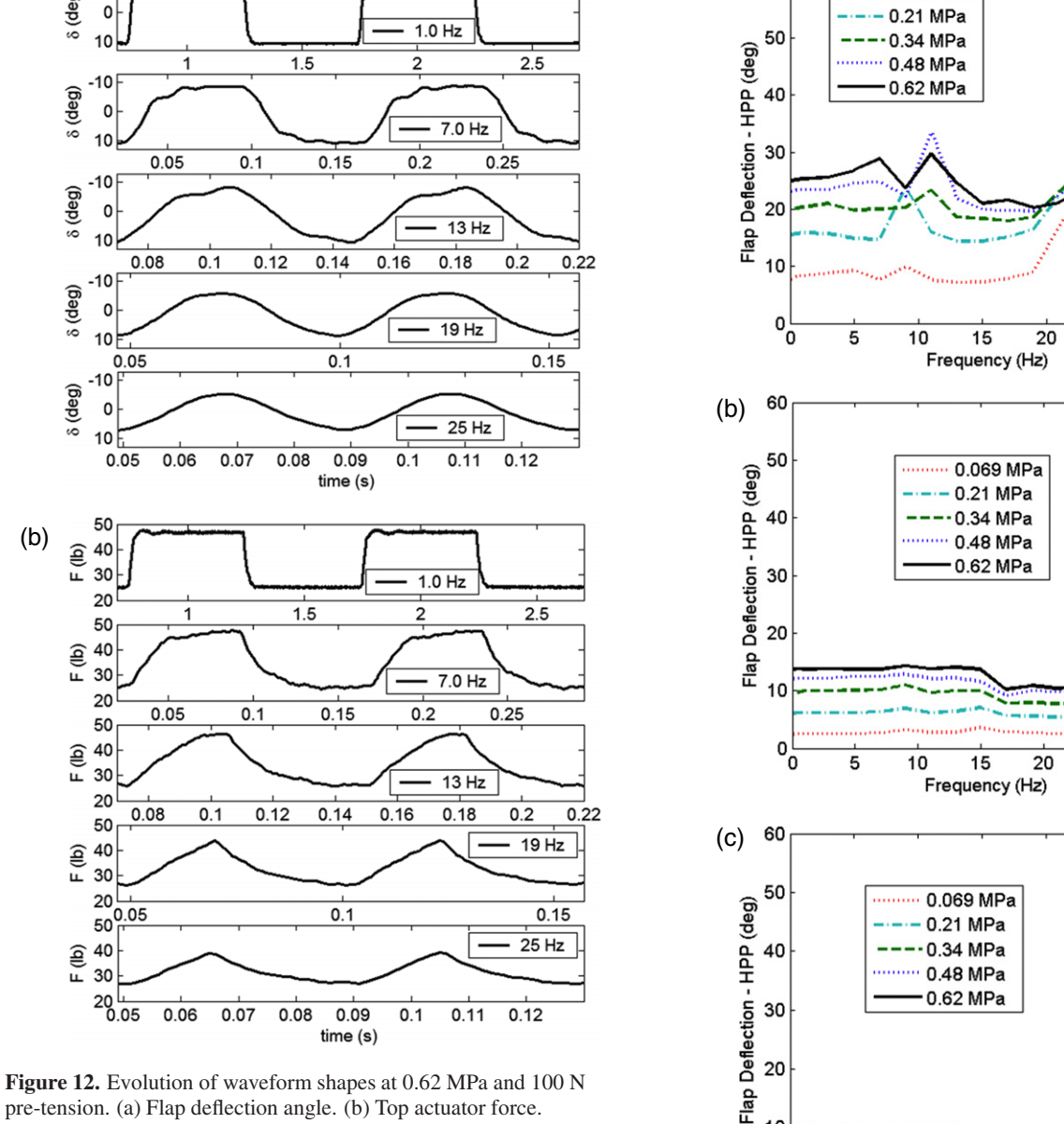
(a)

25

25

30

30



60

0.069 MPa

(a)

pre-tension. (a) Flap deflection angle. (b) Top actuator force.

4.3. Discussion of bench-top measurements

One important result of the bench-top testing was the observation that the system performance was less than originally predicted because of the increased antagonistic hinge force resulting for PAM pre-tension. As discussed above, our ability to meet the desired deflection levels was based on the force levels of a single PAM actuator under 0.62 MPa and 12% pre-strain, or 100 N pre-tension. This original design analysis neglected the opposing actuator force because small deflections were assumed. However, for the chosen actuator size to produce the required force, a significant amount of pre-tension was actually needed. According to the benchtop results of figure 14(c), pre-strain significantly increases the opposing force on the hinge, making the impact of the opposing actuator non-negligible.

The initial analysis states that the system needs 276 N of unopposed force to deflect the flap to $+10^{\circ}$ at a simulated

Figure 13. Maximum unloaded flap deflection as a function of frequency and pressure. (a) 10 N pre-tension. (b) 60 N pre-tension. (c) 100 N pre-tension.

10

15

Frequency (Hz)

20

25

30

0,

5

hinge moment corresponding to Mach 0.3, but as configured at a pre-tension of 100 N, the active PAM generates a maximum of 218 N, while the passive PAM sees nearly 111 N. Underperformance in the active PAM combined with a substantial force required to deflect the passive PAM results in a net hinge moment substantially less than 1.9 N m.

In addition, the design of the moment block created moment arms for the active and passive PAM that changed with flap deflection in a manner that degraded performance. The active actuator's moment arm decreases with increasing

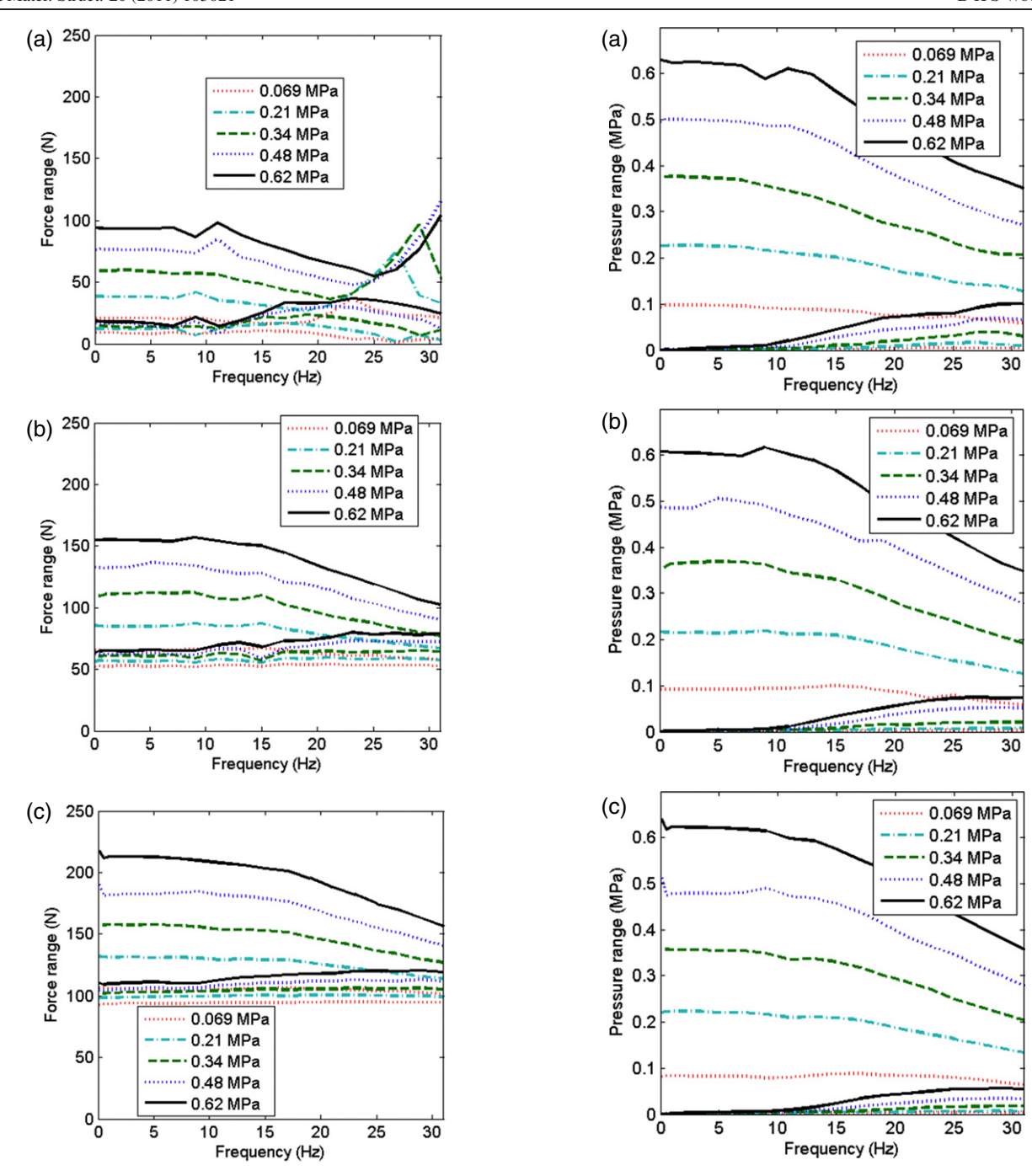


Figure 14. Unloaded actuation force range as a function of frequency and pressure for upper actuator. (a) 10 N pre-tension. (b) 60 N pre-tension. (c) 100 N pre-tension.

Figure 15. Unloaded actuation pressure range as a function of frequency and pressure for upper actuator. (a) 10 N pre-tension. (b) 60 N pre-tension. (c) 100 N pre-tension.

flap deflections, while the passive actuator's moment arm increases. This progressively reduces the effectiveness of the active PAM while increasing the counteracting moment of the passive PAM.

These two factors contributed to produce (quasi-static) flap deflections under load that were about half the expected values. The deflections seen $(\pm 5^{\circ})$ are still significant, especially in comparison to those obtainable with other smart material systems [30]. Additionally, the actuators used were relatively small in comparison to the flap itself, implying that larger PAMs and/or additional antagonistic pairs could be used

to drive the flap with only a modest increase in weight if better performance was desired.

The reduction in flap output with frequency is believed to be the direct result of air flow rate restrictions in the pneumatic supply system. The relevance of this trend is dependent on the intended operating frequency range needed for a given application. Some potential applications, such as helicopter trailing edge flaps, will operate at frequencies on the order of 30 Hz or more. In this case further development of the pneumatic supply system would be desirable to maintain performance. However, for many other applications such

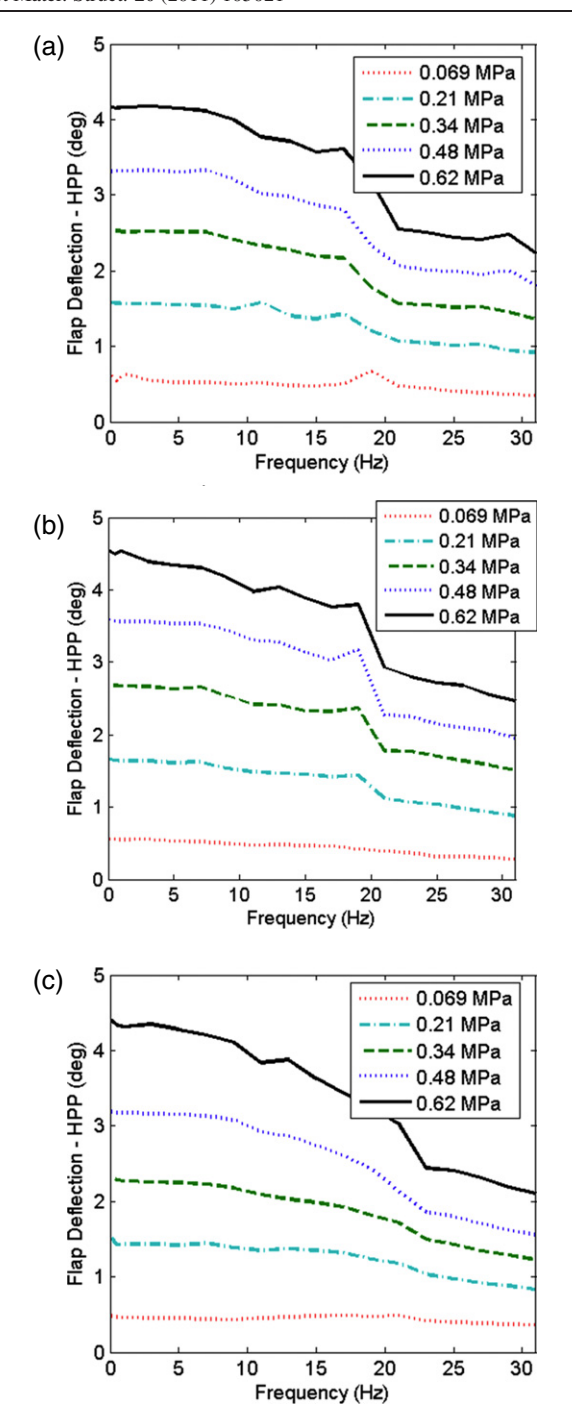


Figure 16. Maximum loaded flap deflection as a function of frequency and pressure. (a) 10 N pre-tension. (b) 60 N pre-tension. (c) 100 N pre-tension.

as UAV control surfaces or wind turbine flaps the operating frequencies will be much lower; making the design of the pneumatic supply system less critical. The importance of properly matching the pneumatic supply system to the PAMs used and the bandwidth desired is clear.

4.4. Free-jet wind tunnel measurements

For the final phase of this experiment, the prototype system was tested in a low speed free-jet wind tunnel. The maximum

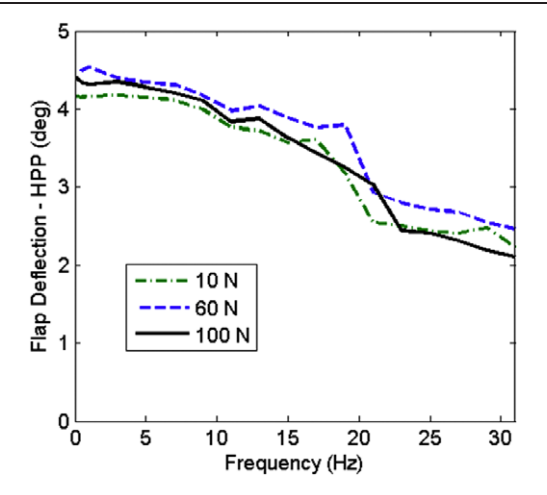


Figure 17. Loaded flap deflections at 0.62 MPa (90 psi).

wind speed of the tunnel used is 45 m s⁻¹. At standard atmospheric conditions, this corresponds to Mach 0.13. While this is substantially slower than the design point for the benchtop testing, it provides a useful demonstration of performance for another potential application: this airspeed is representative of cruising flight (86 knots) for a Predator class UAV [31]. For this evaluation, experiments at three different speeds were conducted: 0 m s^{-1} , $30 \text{ m s}^{-1}(M = 0.085)$, and 45 m s⁻¹ (M = 0.13). The M = 0 case gives an unloaded baseline of the prototype performance with the proper mass and rotational inertia associated with the structure of the flap foam and skin, which was not present in the bench-top experiments. The other two speeds will help illustrate how the system performs under increasing aerodynamic loading. For this testing, a pre-tension of 10 N was chosen based off the bench-top results. The same experimental set-up as shown in figure 10 was used for these experiments, and the interested reader can view a video of some sample tests in the supplementary data. The tests shown in the video are for a wind speed of 30 m s⁻¹ and for a set of discrete actuation frequencies: 0.5, 5, 11, 15, 19, 25 and 31 Hz (see stacks.iop. org/SMS/20/105021/mmedia).

The flap deflection results for all three test conditions are presented in figure 18. Here, the maximum positive angle the flap can attain is displayed over the tested frequency and pressure range.

Related results are provided in figure 19, where the actuator forces that correspond to the flap deflections of figure 18 are shown. For off-resonance frequencies, the forces generated by the actuator are similar for all three speeds. As was the case in the bench-top experiments, this is because actuation force is related primarily to applied pressure, whereas the flap deflection is dependent on both the applied PAM force and external aerodynamic loading. These results show that at 0.62 MPa, 111 N of force can be generated in quasi-static conditions and approximately 90 N can be generated at 25 Hz.

To highlight the effects that wind speed has on the prototype system performance, figure 20 has been included to show results from a single representative pressure for all three wind speeds. The pressure of 0.62 MPa (90 psi) was chosen

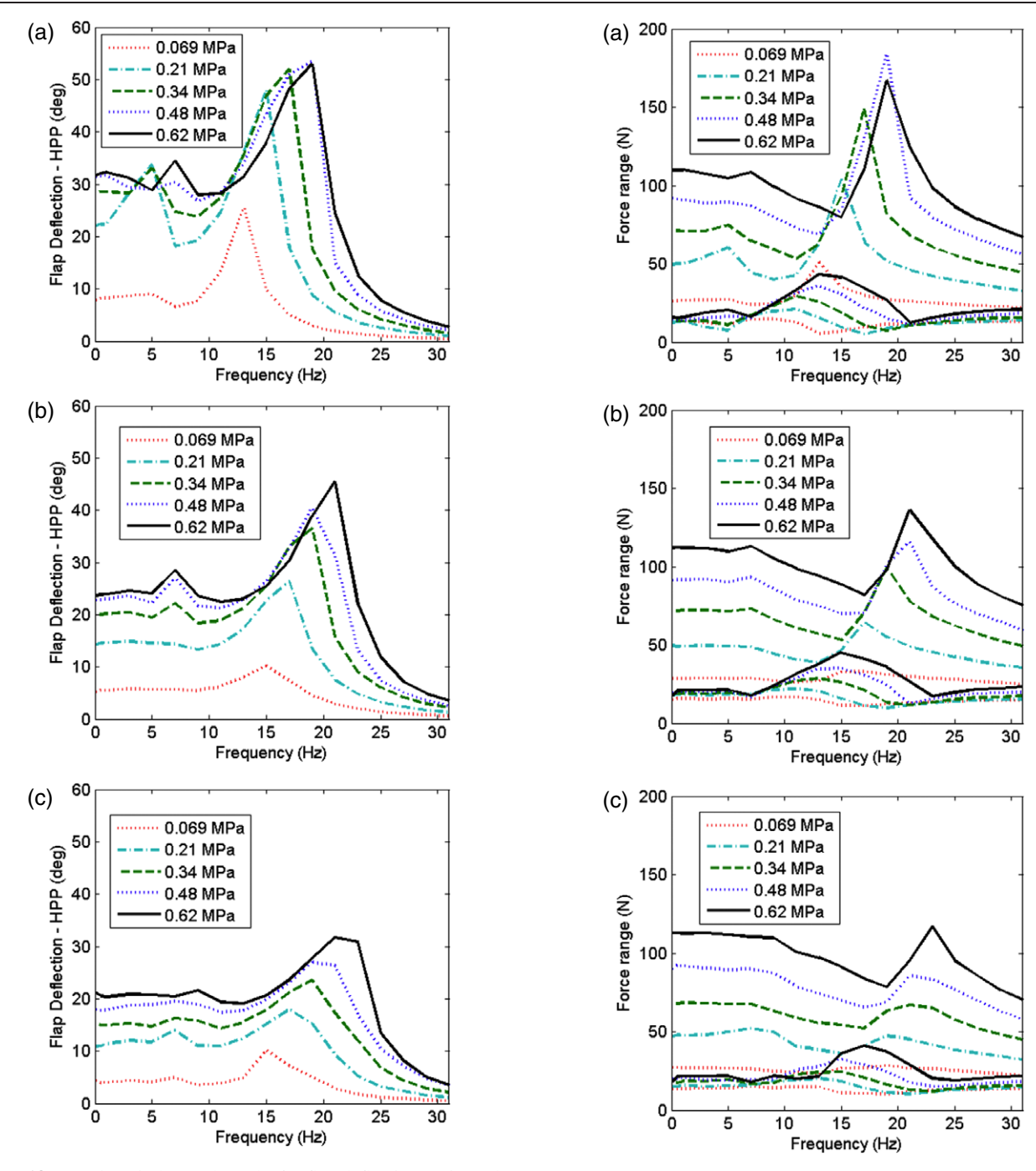


Figure 18. Free-jet wind tunnel results for flap deflection at 6° angle of attack and 10 N pre-tension. (a) 0 m s⁻¹. (b) 30 m s⁻¹. (c) 45 m s^{-1} .

because the maximum performance was achieved. Figure 20 shows that the frequency of the peak angular deflection shifts from roughly 19 to 22 Hz from the baseline unloaded case implements.

to the full speed condition, while the maximum deflection (at resonance) drops from $\pm 55^{\circ}$ to $\pm 31^{\circ}$.

The flap deflections obtained in the wind tunnel fell as expected between the unloaded and simulated M=0.3 bench-top cases, and exhibited similar dynamic characteristics. The same gradual reduction in performance with increasing actuation frequency is visible in the wind tunnel data and again is attributed to a decrease in active PAM pressure coupled with

Figure 19. Free-jet wind tunnel results for force in upper actuator at 6° angle of attack and 10 N pre-tension. (a) 0 m s^{-1} . (b) 30 m s^{-1} . (c) 45 m s^{-1} .

an increase in passive PAM pressure. These wind tunnel results demonstrate that the PAM-driven trailing edge flap system implemented here can produce at least $\pm 20^{\circ}$ in control surface deflections at frequencies up to 24 Hz under aerodynamic loading representative of a medium scale UAV.

5. Conclusions

Pneumatic artificial muscles (PAMs) are a promising alternative to both conventional hydraulic and electric motor actuators, as well as smart material-based technologies, for

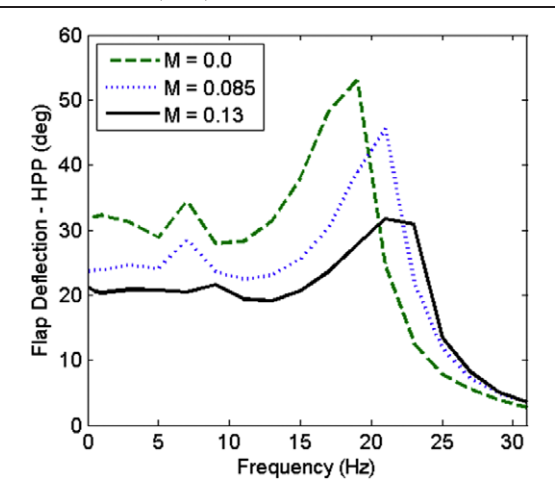


Figure 20. Free-jet wind tunnel deflection angle results at 0.62 MPa (90 psi) for different wind speeds.

control surface actuation. This study produced a first generation prototype proving the feasibility of a trailing edge flap system actuated by antagonistic PAMs.

It was shown that PAMs with an active length of 8 cm and an outer diameter of 1.27 cm (0.5 in) were capable of producing 110 N of blocked force at an operational pressure of 0.62 MPa (90 psi), which was sufficient to actuate the trailing edge flap system examined in this study. These PAMs were then integrated into bench-top and wind tunnel test articles for system evaluations.

- (1) In the bench-top testing, springs were used to simulate aerodynamic loads equivalent to M=0.3 flight, and results showed that $\pm 4^{\circ}$ flap deflection could be achieved for actuation frequencies up to 15 Hz.
- (2) Wind tunnel experiments were conducted at M=0.13 wind speed conditions, and the PAM-based trailing edge flap system deflected the flap $\pm 20^{\circ}$ for actuation frequencies up to 24 Hz.
- (3) It was shown that pre-tension greatly increased the PAM actuator block force. However, because both PAMs in an antagonistic configuration would have the same pre-tension in order to maintain the zero angle, the antagonistic force increases as well, thereby negating any potential benefit.
- (4) System resonance behavior had a significant effect on flap deflections and was observed to be actuation pressure and pre-tension dependent.
- (5) Pneumatic supply system limitations were identified as the key limiter of high frequency performance. In order to maximize the operating bandwidth of future PAM-driven trailing edge flap systems, the maximum available flow rate of the pneumatic supply must meet or exceed the flow rate requirements of the actuators.

In summation, this investigation demonstrates that PAM-driven flap devices produce appropriate levels of block force and free contraction (or free strain) without resorting to dynamic amplification, are lightweight, and are a feasible alternative to conventional control surface actuation technologies.

Acknowledgments

This research was supported by SBIR funding from the US Army Aeroflightdynamics Directorate under contract number W911W6-06-C-0033 (technical monitor: Dr Mark Fulton). The authors also thank Edward A Bubert for assisting with bench-top and wind tunnel testing.

References

- Hall S R and Prechtl E F 1996 Development of a piezoelectric servoflap for helicopter rotor control *Smart Mater. Struct.* 5 26–34
- [2] Straub F K, Ngo H T, Anand V and Domzalski D B 2001 Development of a piezoelectric actuator for trailing edge flap control of full scale rotor blades *Smart Mater. Struct.* 10 25–34
- [3] Lee T and Chopra I 2001 Design of piezostack-driven trailing-edge flap actuators for helicopter rotors Smart Mater. Struct. 10 15–24
- [4] Ardelean E V, Cole D G and Clark R L 2004 High performance 'V-stack' piezoelectric actuator J. Intell. Mater. Syst. Struct. 15 879–89
- [5] Kim J S, Wang K W and Smith E C 2001 High-authority piezoelectric actuation system synthesis through mechanical resonance and electrical tailoring *J. Intell. Mater. Syst.* Struct. 16 21–31
- [6] Epps J J and Chopra I 2001 In-flight tracking of helicopter rotor blades using shape memory alloy actuators *Smart Mater*. *Struct.* 10 104–11
- [7] Strelec J K, Lagoudas D C, Khan M A and Yen J 2003 Design and implementation of a shape memory alloy actuated reconfigurable airfoil J. Intell. Mater. Syst. Struct. 14 257–73
- [8] Nelson C T and Rediniotis O K 2004 An active flap deployment system for blade-disturbance interaction alleviation J. Fluids Eng. 126 1006–14
- [9] Kennedy D K, Straub F K, Schtky L M, Chaudhry Z and Roznoy R 2004 Development of an SMA actuator for in-flight rotor blade tracking J. Intell. Mater. Syst. Struct. 15 235–48
- [10] Fenn R C, Downer J R, Bushko D A, Gondhalekar V and Ham N D 1996 Terfenol-D driven flaps for helicopter vibration reduction Smart Mater. Struct. 5 49–57
- [11] Austin F, Siclari M J, Kesselman M and Weisensel G N 1998 Smart Terfenol-D-powered trailing edge experiment *Proc.* SPIE 3326 282–93
- [12] Chopra I 2002 Review of state of art of smart structures and integrated systems AIAA J. 40 2145–87
- [13] Neal D A, Good M G, Johnston C O, Robertshaw H H, Mason W H and Inman D J 2004 Design and wind-tunnel analysis of a fully adaptive aircraft configuration *Proc. AIAA* Structures, Structural Dynamics, and Materials Conf. (Palm Springs, CA) AIAA-2004-1727
- [14] Poonsong P 2004 Design and analysis of a multi-section variable camber wing MS Thesis Aerospace Department, University of Maryland
- [15] de Marmier P and Wereley N M 2003 Control of sweep using pneumatic actuators to morph wings of small scale UAVs Proc. AIAA Structures, Structural Dynamics, and Materials Conf. (Norfolk, VA) AIAA-2003-1802
- [16] Blondeau J, Richeson J and Pines D 2003 Wind tunnel testing of a morphing aspect ratio wing using a pneumatic telescoping spar Proc. AIAA Structures, Structural Dynamics, and Materials Conf. (Norfolk, VA) AIAA-2003-1718

- [17] Samuel J B and Pines D J 2007 Design and testing of a pneumatic telescopic-wing for unmanned air vehicles AIAA J. Aircraft 44 1088–99
- [18] Kothera C S, Woods B K S, Sirohi J, Wereley N M and Chen P C 2010 Fluid-driven artificial muscles as mechanisms for controlled actuation *US Patent Specification* 7,837,144 (Filed: 11 August 2006. Issued: 23 November)
- [19] Festo Fluidic Muscle DMSP, Product data sheet www.festo. com, cited 10 August 2006
- [20] Daerden F and Lefeber D 2002 Pneumatic artificial muscles: actuators for robotics and automation Eur. J. Mech. Environ. Eng. 47 10–21
- [21] Medrano-Cerda G A, Bowler C J and Caldwell D G 1995 Adaptive position control of antagonistic pneumatic muscle actuators *IEEE Intelligent Robots and Systems Conf.* vol 1 (Piscataway, NJ: IEEE) pp 378–83
- [22] Kornbluh R et al 1998 Electrostrictive polymer artificial muscle actuators IEEE Int. Conf. on Robotics and Automation vol 3 (Piscataway, NJ: IEEE) pp 2147–54
- [23] Caldwell D G, Tsagarakis N and Medrano-Cerda G A 2000 Bio-mimetic actuators: polymeric pseudo muscular actuators and pneumatic muscle actuators for biological emulation *Mechatronics* 10 499–530

- [24] Schulte H F 1961 The characteristics of the McKibben artificial muscle *The Application of External Power in Prosthetics* and Orthotics (Washington, DC: National Academy of Sciences–National Research Council) pp 94–115 (Pub. 874, App. H)
- [25] Kothera C, Jangid M, Sirohi J and Wereley N M 2009 Experimental characterization and static modeling of McKibben actuators ASME J. Mech. Des. 131 091010
- [26] Chou C P and Hannaford B 1996 Measurement and modeling of McKibben pneumatic artificial muscles *IEEE Trans*. *Robot. Autom.* 12 90–102
- [27] Klute G and Hannaford B 1998 Fatigue characteristics of McKibben artificial muscle actuators *Proc. IROS 1998* (*Victoria, BC*) pp 1776–82
- [28] Abbott I H and von Doenhoff A E 1959 *Theory of Wing Sections* (New York: Dover)
- [29] Etkin B 1982 Dynamics of Flight 2nd edn (New York: Wiley)
- [30] Giurgiutiu V 2000 Review of smart-materials actuation solutions for aeroelastic and vibration control *J. Intell. Mater. Syst. Struct.* 11 525–46
- [31] Yenne B 2004 Attack of the Drones: A History of Unmanned Aerial Combat (St Paul, MN: Zenith Press)